AIAA JOURNAL
Vol. 31, No. 10, October 1993

Space Marching Calculations About Hypersonic Configurations Using a Solution-Adaptive Mesh Algorithm

Albert D. Harvey* and Sumanta Acharya†
Louisiana State University, Baton Rouge, Louisiana 70803
and
Scott L. Lawrence‡
NASA Ames Research Center, Moffett Field, California 94035

A solution-adaptive marching algorithm is developed and applied to a three-dimensional parabolized Navier-Stokes equation solver. The resulting algorithm obtains accurate solutions by using a spatial-marching/adaptive-grid procedure. The adaptation step redistributes grid points line by line in both crossflow directions, with grid point motion controlled by forces analogous to tensional and torsional spring forces with the tensional force proportional to the error measure or weighting functions. The solution-adaptive marching procedure is applied to the hypersonic flow about two generic aircraft configurations. The first of these is an all-body-type geometry with elliptical cross sections and is studied at angles of attack of 0, 5, and 15 deg. The second geometry is a generic blended-wing-body design. Results are presented that demonstrate the improvements in flowfield resolution obtainable with the solution-adaptive marching procedure over conventional fixed grid techniques. Computed pitot pressure profiles obtained using the solution-adaptive algorithm show improved agreement with experimental data compared to predictions obtained using a fixed grid.

Introduction

THIS paper describes the continued development and application of a solution-adaptive grid algorithm coupled with a parabolized Navier-Stokes (PNS) solver. In Ref. 1, the present authors presented a two-dimensional adaptive grid scheme, and in Ref. 2 they presented a three-dimensional solution-adaptive procedure and applied it to the flow over a yawed circular cone. In applying the method of Ref. 2 to more complex geometries, it was found to be necessary to improve the method through modifications that provide a smooth adapted grid at each step and that permits an easy application of the procedure to complex geometries. The improvements to the procedure in Ref. 2 are described in this paper, and the improved procedure is applied toward the solution of the flow over two complex geometries.

Truncation error in any finite difference scheme is proportional to the grid spacing raised to the power of the order of accuracy. Adaptive grid techniques provide a means for improving the accuracy of numerical solutions to field equations by adjustments in the grid point locations. Numerous studies on adaptive grid techniques are currently available. Thompson,[3] Hawken,[4] and Moukalled[5] independently provide complete surveys of the most widely accepted methods.

The present solution-adaptive grid technique uses a spring analogy to model grid point motion. Gnoffo,[6] Nakahashi and Deiwert,[7,8] Davies and Venkatapathy,[9] and Djomehri and Deiwert[10] have all made significant contributions to adaptation methods that are similar in their basic ideas to the present one in that they employ the tension and torsion spring analogy to formulate the equations that yield the adapted grid point positions. The present work, however, makes a number of distinct and unique contributions that make the method different from the other reported contributions. Some of these important contributions of the present work are discussed next.

The present solution-adaptive grid algorithm is embedded in a PNS solver and obtains accurate numerical solutions in a single pass. At each downstream step, an improved solution is obtained on an adapted grid immediately after grid adaptation is performed.

The calculation of error estimates or weighting functions used to control grid point redistribution is based on an algorithm whereby an error measure (generally a weighted combination of the gradient or curvature) is computed at all points and then normalized. The largest normalized gradient is then chosen to represent the weighting function at each point along a coordinate line. Thus, during grid adaptation, equal consideration is given to all variables; for instance, pressure is changing rapidly in one region of the flow but may be unimportant in other regions, where other variables may be changing significantly. Because of spatial limitations here, the reader is referred to Refs. 1 and 2 for a more complete description of the weighting function selection procedure.

Three-dimensional applications of solution-adaptive grid techniques have been reported by Nakahashi and Deiwert[8] and Djomehri and Deiwert,[10] who have incorporated the use of two torsional force terms in the grid adaptation equations. A user-specified parameter is required for each term. In Harvey et al.[2] this technique was employed with limited success to adapt the grid for the flow over cones at angles of incidence. It was difficult to find appropriate values for the torsion parameters that produce an adapted grid that is suitably smooth for obtaining a numerically stable second solution step in the present solution-adaptive marching scheme. A different torsional formulation presented in Ref. 2 was then devised in an attempt to provide a method that allowed a wider range of appropriate adaptation parameters. In the formulation of Ref. 2, a single torsion parameter is specified and the torsional dependence is divided into two components by proportioning the relative magnitudes of the streamwise and crossflow torsion terms with the relative grid scales in the respective directions. Although this technique produces satisfactory results for relatively simple geometries such as cones, it was found to be inadequate for more complex situations.

In an attempt to further improve the relationship between neighboring grid lines in the adaptation equations, a different approach is devised in the present paper. This technique involves defining a single grid reference position, eliminating one of the torsional

Presented as Paper 91-3237 at the AIAA 9th Applied Aerodynamics Conference, Baltimore, MD, Sept. 23–26, 1991; received Aug. 1, 1992; revision received Feb. 25, 1993; accepted for publication March 19, 1993.

*Graduate student; currently Senior Research Engineer, Dow Chemical USA R&D, Plaquemine, LA 70765. Member AIAA.
†Professor, Department of Mechanical Engineering. Member AIAA.
‡Research Scientist, Applied Computational Fluids Branch. Member AIAA.

force terms in the adaptation equations altogether, and including a second parameter (to be described later) to proportion the grid reference positions from the crossflow and streamwise directions to define a single grid reference position. Thus, with this formulation, only one torsional force term appears in the adaptation equations. This approach was found to be more robust in that a wider range of values for the torsional parameter exists that produce a smooth adapted grid for the second solution step of the solution-adaptive marching procedure.

Another contribution of the present work is the development of a grid-fitting scheme for three-dimensional flows similar in principle to that presented in Ref. 1 for two-dimensional flows. For complex three-dimensional problems it is often difficult to define a grid that is accurately aligned with the shock structure. If the grid is not aligned to some extent, grid adaptation using the present technique is very difficult. Grid lines tend to distort in the freestream. The grid-fitting algorithm eliminates these problems by accurately aligning the outer grid line with the outermost shock. As a result, the shock remains stationary relative to the grid, and furthermore, a maximum grid density is obtained in the region of interest. This feature also improves the performance of the adaptive grid algorithm, eliminating the severe grid distortions that appear without the use of the grid-fitting scheme.

Solutions to the PNS equations are obtained by marching in space rather than time and therefore are obtained much more efficiently than solutions to the time-dependent Navier-Stokes equations. The present flow solver, developed by Lawrence[11] and Lawrence et al.[12,13] involves the integration of the PNS equations and incorporates a steady version of Roe's approximate Riemann solver[14] for the modeling of the inviscid fluxes.

Solution-Adaptive Procedure

The present grid-adaptation technique is based on the error equidistribution method and involves the redistribution of grid points such that an error measure, which is generally proportional to $(\Delta s)^n$ multiplied by a function of the flowfield variable derivatives [i.e., $\Delta s^n \omega(\phi, \phi', \ldots, \phi^n)$], is equally distributed over a coordinate line. In simplistic terms, this can be written as

$$w_i \Delta s_i = K$$

The grid interval Δs_i is defined as the distance between adjacent grid points along a line of constant computational coordinate, and the weighting function w_i is defined as a function of a selected normalized flow property $\bar{f}$ such that

$$w_i = 1 + A\bar{f}_i^B$$

where A and B are constants related to the specified maximum and minimum grid spacings and are calculated from user-requested maximum and minimum grid spacings Δs_{MAX} and Δs_{MIN}. The normalized flow property $\bar{f}$ is obtained from a number of user-selected dependent flow variables. The reader is referred to Refs. 1 and 2 for complete details on the weighting function selection procedure.

In a typical space-marching algorithm, the grid plane at the current marching station and the grid plane at the next marching station a distance $\Delta\xi$ downstream make up a computational slab. When performing the space-marching solution procedure, it is necessary to be able to define the crossflow geometry of the body at any arbitrary streamwise location. However, a typical surface grid is composed of a finite number of specified crossflow surface sections (ξ intervals), and the marching step size $\Delta\xi$ generally differs appreciably from the size of these surface grid ξ intervals. Therefore, crossflow grid planes are first constructed at locations corresponding to each ξ interval on the input surface grid. This can be done during the marching process, one by one, as each new ξ interval is encountered using conventional grid-generation techniques. The grid planes at the actual marching stations, which are grid planes intermediate to the grid planes at the surface ξ intervals, can then be obtained by linear interpolation between the grid planes on either side.

Once the grid plane at the current marching station is adapted, the task arises of building a grid plane at the next marching station. These two adjacent grid planes must be sufficiently aligned with one another to make up a computational slab that will permit accurate numerical integration of the flow equations. As the solution-adaptive marching scheme proceeds downstream, the grid becomes more aligned with the flowfield structure. As the marching planes become more adapted, and if the surface geometry changes appreciably in the marching direction, the task of constructing an adjacent grid plane at the next marching station a distance $\Delta\xi$ downstream of the newly adapted marching station can become increasingly complex. In fact, this is the major obstacle in implementing an effective three-dimensional solution-adaptive marching procedure.

In the marching solution-adaptive grid procedure developed in Ref. 2, the grid plane at each subsequent marching station downstream of the current marching station is obtained by linear interpolation between the adapted grid plane at the current marching station and the grid plane at the next ξ interval of the surface grid downstream. The grid plane at the next ξ interval of the surface grid is updated after adaptation of the current marching station by performing a sequence of one-dimensional interpolations along each coordinate line separately. Thus, the two planes between which a preliminary crossflow plane is interpolated are sufficiently aligned with each other so that the linear interpolation produces a grid plane at the next marching station that is aligned with the current marching station. In this manner, the complex problem of three-dimensional grid-point interpolation is avoided.

This method of aligning the upstream and downstream sides of the computational slab in preparation for numerical integration was, however, found to be restricted to relatively simple bodies whose surface geometry changes at some constant rate (such as the right circular cone of Ref. 2) and is not suited to more complex configurations such as those contained in the present work.

In this paper, an improved procedure is developed for generating a preliminary crossflow grid plane at the downstream location. The crossflow grid at each marching station is obtained from a downstream projection of the grid at the previous marching station. Instead of trying to align the downstream grid plane with the adapted grid plane and then performing an interpolation between these two grid planes to construct the computational slab (as described earlier for the cones of Ref. 2), we found that a more general procedure (applicable to more general three-dimensional

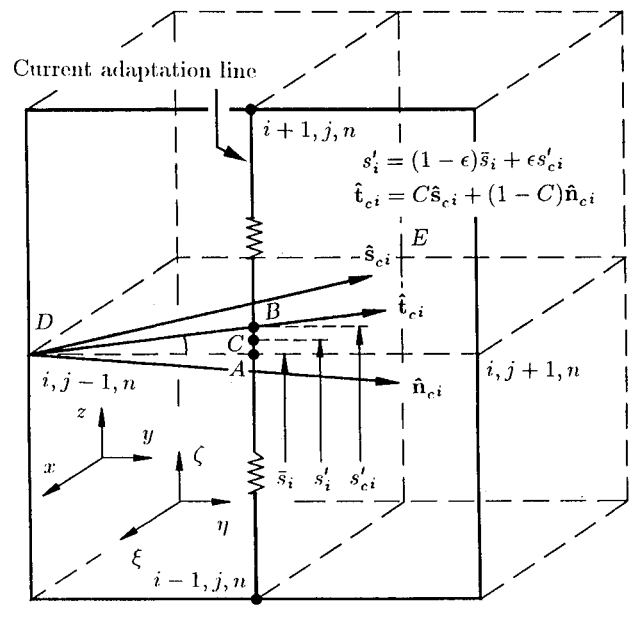

Fig. 1 Adaptive mesh geometry.

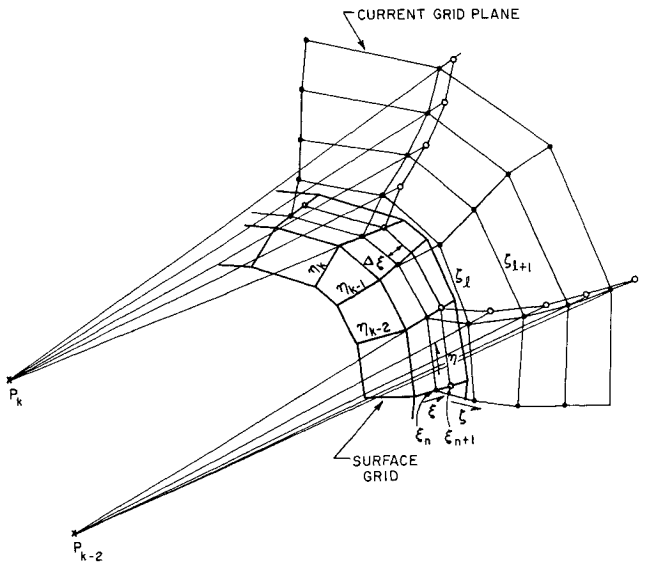

Fig. 2 Downstream projection of adapted grid plane.

geometries) is to project the adapted grid plane at the current marching station downstream to the next marching station using the fixed surface grid as a guide. The only additional information needed (in addition to a complete surface grid) is that concerning how far out into the freestream the next grid plane should extend. This information is obtained with a grid-fitting scheme that monitors the far-field flow structure at each marching station and keeps the outer edge of the grid in the freestream. The three-dimensional grid-fitting scheme and the improved grid projection techniques are described in more detail later and represent two important contributions of this paper.

In the next section, a slightly different three-dimensional formulation of the grid adaptation equations than that presented by Harvey et al.[2] is presented. The new formulation incorporates a single torsional force term and provides improvements in grid smoothness and algorithm robustness.

Grid Skewness Control

By performing a force balance along a constant ζ line on the system of tensional and torsional springs about the point (i, j, n) in Fig. 1, we obtained the following system of equations:

$$w_i(s_{i+1} - s_i) - w_{i-1}(s_i - s_{i-1}) - K\theta_i = 0 \tag{1}$$

where s_i is the resulting length of the current adaptation line up to the new grid point location, and K is a proportionality constant. The torsion angles θ_i can be approximated as $\theta_i \approx (s_i - s_i')/|DB|$, where $|DB|$ is the distance from point D to point B in Fig. 1. The quantities s_i' are defined as the total length of the coordinate line up to the location of the grid reference location (point C of Fig. 1) that is determined, as described later, from neighboring grid lines. The term $K\theta_i$ represents a force on the grid point toward the reference point corresponding to s_i', and it therefore represents the influence from neighboring grid points.

By substituting the expression for θ_i into Eq. (1) and rearranging and defining $\tau_i = K/|DB|$, we obtained the following linear system:

$$w_{i-1}s_{i-1} - (w_{i-1} + w_i + \tau_i)s_i + w_i s_{i+1} = -\tau_i s_i' \tag{2}$$

The previous formulation differs from the formulation of Ref. 2 in that only one torsional force term is present. The use of a single torsional force term has distinct advantages over the approach of Ref. 2, which consists of multiple torsional terms and can often produce opposing torsional forces and cause inconsistent grid point movement. The single torsion term $\tau_i s_i'$ of the present formulation must now contain grid information from both streamwise and crossflow directions. The calculation of both τ_i and s_i' is described next.

Equation (2) indicates that as the term τ_i becomes large, the equilibrium position of the ith grid point approaches the position corresponding to the location s_i'. This location represents the equilibrium position of the individual torsional springs projecting from neighboring grid lines. Consequently, a value of s_i' much different from $\bar{s}_i$, the positions of the grid points before grid adaptation, can result in excessive movement of grid points, even without any input from the error measure. The initial grid point position $\bar{s}_i$, before the grid adaptation step, corresponds to the grid point position that results from the downstream projection of the grid at the $n-1$ marching station to the nth marching station. The downstream projection of the current grid plane to the next marching station is described in a later section.

To achieve precise and bounded grid point movement, the values of s_i' must remain close to the preliminary grid point positions $\bar{s}_i$, and at the same time the values of τ_i of Eq. (2) must be chosen so as to hold the grid close to these locations. Values of τ_i that are too large can smother the effect of the weighting functions, causing the grid to move independent of the solution, whereas values that are too small permit excessive movement.

To make all of the terms of Eq. (2) of the same order of magnitude at each point along the adaptation line, τ_i is defined in the following manner:

$$\tau_i = \lambda(w_{i-1} + w_i)\bar{\alpha}_i \tag{3}$$

where λ is a user-defined stiffness parameter and $\bar{\alpha}_i = \alpha_i/\alpha_{\min}$ is the aspect ratio of the grid cell normalized with respect to the minimum cell aspect ratio. Each aspect ratio is computed using the notation of Fig. 1 as follows:

$$\alpha_i = \frac{s_{i+1,j,n} - s_{i-1,j,n}}{|DB|}$$

The use of τ_i from Eq. (3) in Eq. (2) ensures that all terms of Eq. (2) are of the same order of magnitude for all points along the line. With this formulation, equal consideration is given to both the weighting functions and the surrounding grid geometry in deciding how the grid points should move.

The preliminary grid point positions $\bar{s}_i$ obtained by projecting the upstream grid plane to the current location (point A of Fig. 1) do not necessarily satisfy the requirements for grid orthogonality and straightness in the crossflow direction. For satisfying orthogonality and straightness requirements in the crossflow direction, grid torsional reference positions s_{ci}' are defined, as described

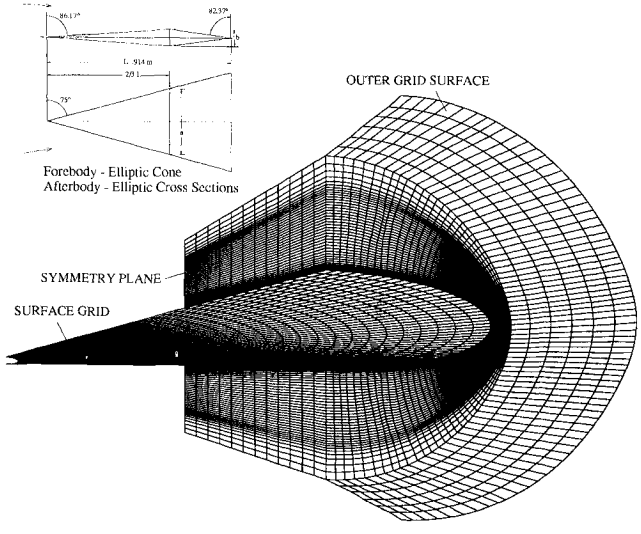

Fig. 3 Sectional view of solution-adaptive and grid-fitted computational grid. Location and direction of viewpoint indicated by the arrows in the inset (α = 0 deg, M_∞ = 7.4, $Re_{\infty,L}$ = 15 × 10^6, 151 × 90 crossflow grid).

later. The net torsional reference positions s'_i of Eq. (2) are the positions the grid points should take based on considerations of orthogonality and straightness both in the streamwise direction (specified by $\bar{s}_i$) and in the crossflow direction (specified by s'_{ci}). Thus, the net torsional reference positions s'_i are defined as

$$s'_i = (1-\varepsilon)\bar{s}_i + \varepsilon s'_{ci} \tag{4}$$

where ε is a proportionality constant. As mentioned in the preceding section, the τ_i values can be chosen so that the solution to Eq. (2) yields s_i values that are in the neighborhood of the corresponding s'_i values. A value of zero assigned to ε neglects crossflow torsional dependence, whereas a value of unity permits the grid to move without regard to the streamwise grid surface. Obviously, either of these extremes would quickly produce unacceptable results. Small values of ε produce an acceptable degree of grid movement with respect to the grid plane upstream of the current marching station, resulting in sufficient alignment between the two grid planes. However, values too small can cause grid irregularities in the crossflow direction. A value of $\varepsilon = 0.3$ was used for all computations in the section to follow.

The quantities s'_{ci} represent the positions the ith grid point must take so that the grid acquires the desired amounts of straightness and orthogonality in the crossflow direction. The position s'_{ci} is defined as the intersection point of the crossflow torsion vector $\hat{t}_{ci}$ and the current adaptation line (point B of Fig. 1). The crossflow torsion vector $\hat{t}_{ci}$ is computed in the same manner as in Ref. 2 by combining user-specified contributions of grid orthogonality and straightness in the crossflow direction:

$$\hat{t}_{ci} = C\hat{s}_{ci} + (1-C)\hat{n}_{ci} \tag{5}$$

where C can range from zero to unity. A value close to zero enforces more orthogonality whereas values closer to unity provide more grid straightness. The straightness vector $\hat{s}_{ci}$ is defined as a vector from the point $(i, j-2, n)$ to the point $(i, j-1, n)$ of Fig. 1. The orthogonality vector $\hat{n}_{ci}$ is defined as an average of vectors normal to the current grid line and the neighboring line in the crossflow plane.

To ensure that s'_{ci} is monotonically increasing and to provide further grid point motion control, the point B is limited to $\frac{1}{2}\Delta s_k$, where Δs_k is either the distance from the point $(i+1, j, n)$ to the point (i, j, n), if the torsional vector crosses above point A as in Fig. 1, or is the distance from the point (i, j, n) to the point $(i-1, j, n)$, if $\hat{t}_{ci}$ crosses below point A. This procedure is also discussed in Ref. 2.

An important difference in the present formulation for the torsional dependence and that developed in Ref. 2 is that, in the present work, the reference positions from the streamwise and crossflow directions are combined into a single quantity s'_i using an additional parameter. In Ref. 2 an attempt was made to combine the torsional parameters while maintaining two independent reference positions for each grid point. Having two torsional terms driving the grid points toward two different reference positions can lead to an irregular grid point motion. The present formulation overcomes this difficulty and, as later calculations will show, provides a smooth adapted grid.

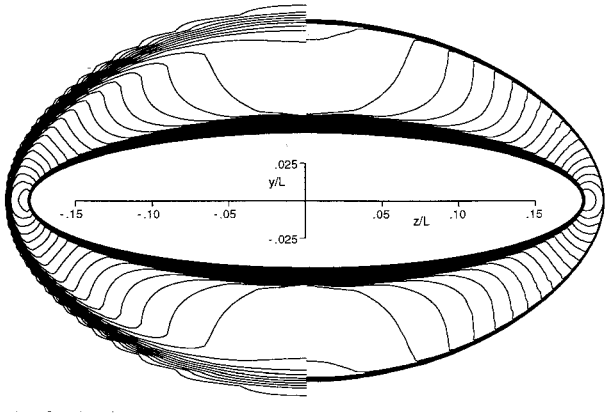

Fig. 4 Comparison of computed Mach number contours; left half, fixed grid; right half, solution adaptive and grid fitted ($\alpha = 5$ deg, $M_\infty = 7.4$, $Re_{\infty,L} = 15 \times 10^6$, $x/L = 0.667$).

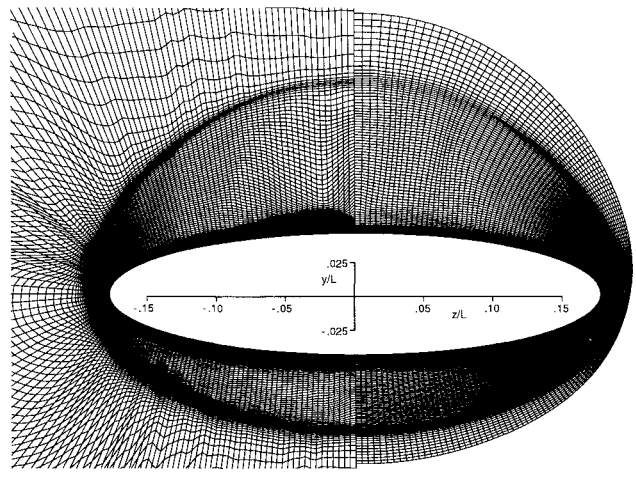

Fig. 5 Comparison of crossflow computational grid planes; left half, solution adaptive; right half, solution adaptive and grid fitted ($\alpha = 5$ deg, $M_\infty = 7.4$, $Re_{\infty,L} = 15 \times 10^6$, $x/L = 0.667$, 151×90 crossflow grid).

Three-Dimensional Grid-Fitting Procedure

This section outlines the procedures by which the total height of the grid is estimated at each marching station and the steps used to project the grid plane at the current marching station to the next marching station. This feature of the present procedure, although presented earlier in Ref. 1 for two-dimensional flows, required major extensions for the three-dimensional situations of interest in this paper.

The solution-adaptive grid-fitting algorithm begins with an initial grid plane of data at the current marching station. This grid plane must be projected downstream to form a computational slab on which numerical integration can be performed. The first step in this projection process is to determine how far out into the freestream the next grid plane must extend. Each η-coordinate line at the current marching station is searched in the ζ direction to find the innermost position of freestream conditions and is clipped (or extrapolated to) a prescribed distance above this location. The resulting new η-ray lengths are first smoothed to minimize inconsistencies in the position of the outer grid line, and then, using a few of these η-line lengths as control points, a spline is fitted to form a temporary new outer grid line at the current marching station. This new grid line is then projected forward to the next marching station using a conical projection from a point far upstream.

Downstream Grid-Plane Projection

At this point in the grid projection process, we now have, in addition to the plane of data at the current marching station and the surface grid, an outer grid line that serves as a far-field grid boundary at the next marching station. The next task is to project the interior of the grid plane at the current marching station (upstream side of the computational slab) to the next marching station (downstream side of the computational slab) in such a manner to ensure that the two sides of the resulting grid slab are uniformly aligned. Figure 2 illustrates a typical grid plane at the current marching station extending outward from the current ξ section of the surface grid. Solid circles are used to represent grid points in the current marching station, and open circles denote grid points (projected points) in the next marching station. To construct the grid plane at the next marching station, each kth point on the ξ_n line of the surface grid is extended a distance far upstream. For example, the point $(\xi_n, \eta_k, 0)$ of the surface grid is extended to the point p_k of Fig. 2, which is defined here as the kth projection point, by extrap-

olating upstream the straight line segment joining the surface points $(\xi_{n+1}, \eta_k, 0)$ and $(\xi_n, \eta_k, 0)$. In this manner, each of the surface grid points in the current marching station at ξ_n are projected backward to construct corresponding projection points. All of the projection points are restricted to lie in a common ξ = const plane far upstream. The kth projection point p_k is then used as a reference from which each grid point along the kth η line in the current marching station is projected linearly into the next marching station. This is done by extending a ray from the kth projection point of Fig. 2, through each of the (ξ_n, η_k, ζ_l) grid points along the η_k line in the current marching station to a distance $\Delta\xi$ downstream.

If the plane of projection points is sufficiently far upstream such that $\Delta\xi/(\xi_n - \xi_p) \ll 1$, where ξ_p is the ξ position of the plane containing the projection points, then the resulting η line projected

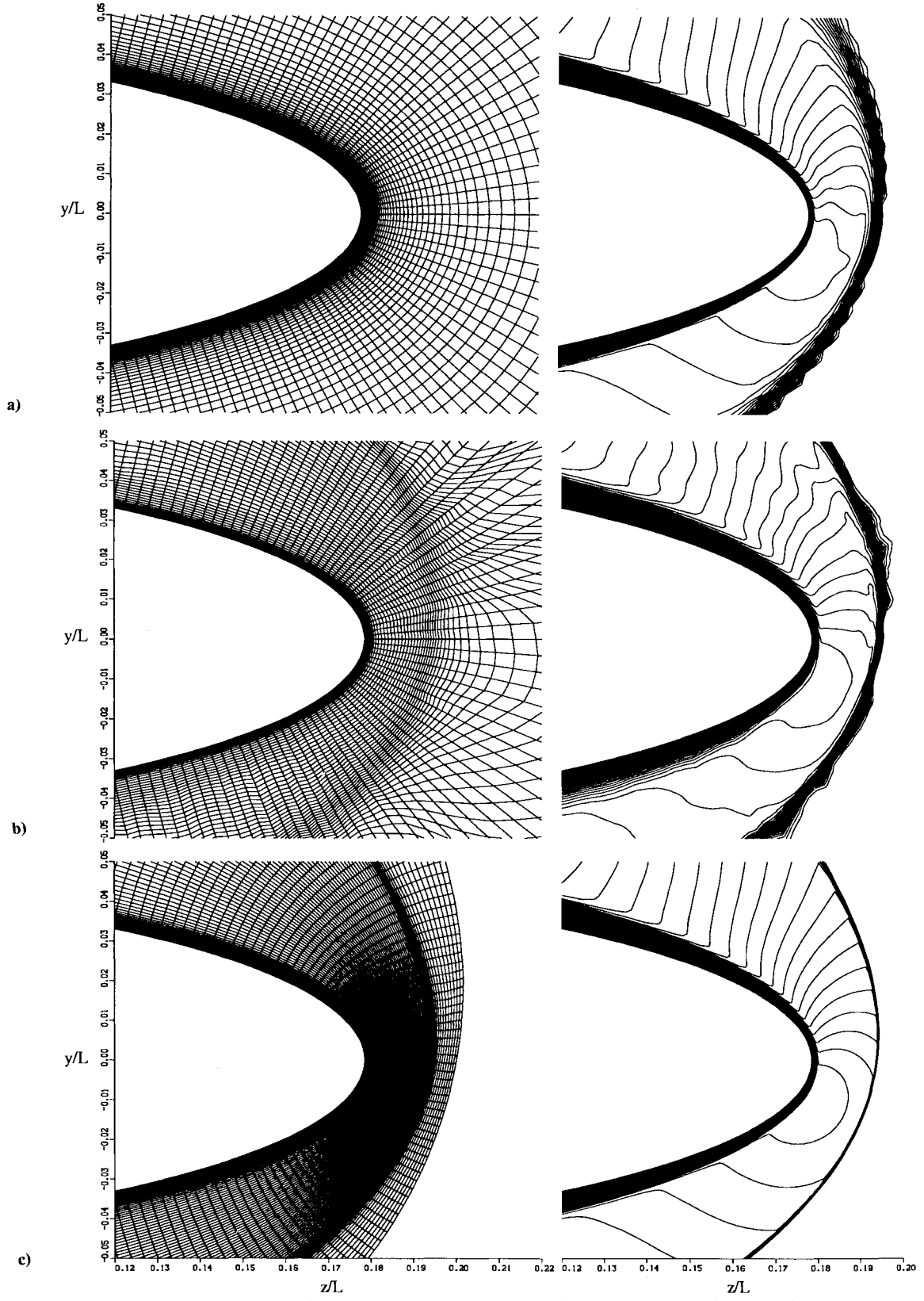

Fig. 6 Comparison of grids and Mach number contours: a) fixed grid, b) adapted, without grid fitting, and c) adapted and grid fitted (α = 5 deg, M_∞ = 7.4, $Re_{\infty,L} = 15 \times 10^6$, x/L = 0.667, 151 × 90 grid).

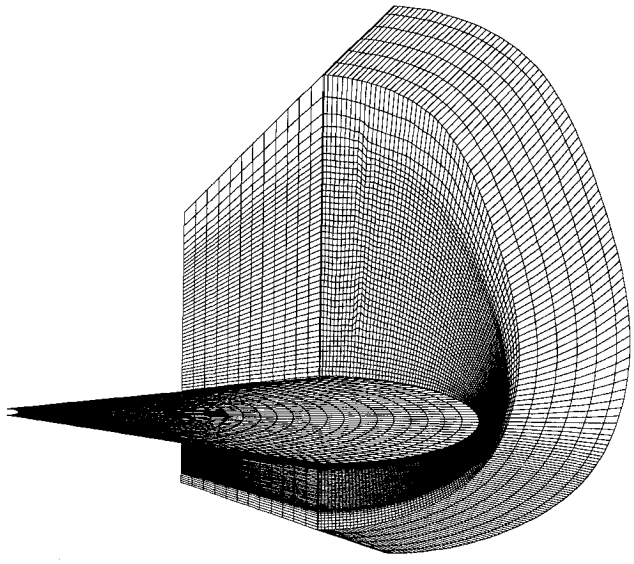

Fig. 7 Sectional view of solution-adaptive and grid-fitted computational grid. Viewpoint location and direction same as Fig. 3 (α = 15 deg, M_∞ = 7.4, $Re_{\infty,L} = 15 \times 10^6$, x/L = 0.667, 151 × 90 crossflow grid).

into the downstream marching plane will have the same shape as the corresponding η line in the current marching plane. Once all of the η lines have been projected downstream in this fashion, a stretching procedure is performed to connect the outer edge of the grid at the new station to the grid-fitted outer line obtained as described previously. Recall that the grid-fitted outer line is the new position of the far-field grid boundary as determined by the grid-fitting procedure, each point of which was projected downstream from a common point far upstream.

In addition to providing an estimated height above the body for projecting the grid downstream, the grid-fitting scheme has been found to assist in providing improvements in the performance of the adaptive grid algorithm. For complex three-dimensional external flows, grid-skewing problems can arise when adapting the grid using the adaptive grid techniques outlined in the previous section if the shape of the grid differs too severely from that of the evolving bow shock. If a large number of grid points are initially in the freestream, outside the bow shock, then grid points will cluster in the vicinity of the bow shock. Any points outside the shock are in a region of constant flowfield properties (i.e., freestream conditions). As the solution proceeds downstream and the adaptation procedure draws grid points into the steep gradient of the bow shock, the outer grid lines tend to kink. The use of the grid-fitting scheme keeps the shape of the grid accurately aligned with the outer shock, producing a degree of resolution that can only be rivaled with the use of a shock-fitting algorithm. This advantage, brought about by the use of the grid-fitting algorithm, will be made more apparent with the use of illustrations in the next section.

Results

Ames All-Body Vehicle

The three-dimensional solution-adaptive PNS algorithm is tested for the hypersonic flow over the all-body configuration with elliptical cross sections shown in the inset of Fig. 3. The flowfield conditions were chosen to match those of the experimental and computational study conducted by Lockman et al.[15] These conditions are as follows: the Reynolds number is $Re_L = 15 \times 10^6$, the freestream Mach number is $M_\infty = 7.4$, the freestream temperature is $T_\infty = 61.5$ K, the wall temperature is $T_w = 311.1$ K, the specific heat ratio is $\gamma = 1.4$, and the Prandtl number is $Pr = 0.72$, where L = 0.9144 m is the total length of the model. As in Ref. 15, a turbulent flow of a perfect gas is assumed, and the eddy viscosity is modeled using the algebraic turbulence model of Baldwin and Lomax,[16] with transition to fully turbulent flow assumed at $x/L = 0.05$. The value of y^+ for the first point off the wall varied between 1–4 for all fixed grid and solution-adaptive, grid-fitted computations. Since the wall spacing for the solution-adaptive and grid-fitted computations was held close to that for the fixed grid computations, y^+ was approximately the same for both solution-adaptive and fixed grid computations. Without the grid fitting, the solution-adaptive algorithm tended to pull the grid away from the wall, increasing the y^+ values.

For each angle of incidence, a conical stepback procedure was performed on an initial grid plane at $x/L = 0.05$ obtained by a hyperbolic grid-generation procedure. Once a converged conical starting solution was obtained, the grid-fitting algorithm was used to fit the outer grid line to the shock. For each angle of incidence case, the cross flow grid plane consisted of 151 grid points in the circumferential direction and 90 grid points in the radial direction.

After a suitable starting solution was obtained using the stepback procedure, the solution-adaptive, grid-fitting, and marching procedure was then employed with a marching step size of 10^{-3} to an x/L location of 0.8 for each angle-of-incidence case. Circumferential adaptations were performed by sweeping from the body surface outward, whereas the direction of the radial adaptation sweeps alternated, sweeping one marching station from the windward to the leeward side and the next station from the leeward to windward side. Alternating the direction of the radial adaptations improved the grid smoothness, allowing grid orthogonality and straightness information to propagate from both sides of the grid.

Adaptation along each crossflow direction (circumferential or radial) required the specification of certain adaptation parameters. The subscripts η and ζ are used, respectively, to delineate the parameters employed along the circumferential and radial directions.

All adaptation parameters used for the present studies were given identical values for each angle-of-incidence case. The maximum and minimum allowable grid spacings were given the following values: $(\Delta s_{MAX})_\zeta/\Delta s_{ave} = 2.5$, $(\Delta s_{MIN})_\zeta/\Delta s_{ave} = 0.5$, $(\Delta s_{MAX})_\eta/\Delta s_{ave} = 2.0$, and $(\Delta s_{MIN})_\eta/\Delta s_{ave} = 0.5$, where Δs_{ave} is the average grid spacing along the adaptation line. The C_ζ and C_η are the grid straightness to orthogonality parameters used for the radial and circumferential adaptations and were given values of 0.7 and 0.4, respectively. The torsional parameters λ_ζ and λ_η of Eq. (3) were given values of 2×10^{-3} and 25, respectively. Mach number, pressure, and density were used as the adaptation variables.

Figure 3 shows the longitudinal sectional view and a cross-sectional view at one streamwise location of the resulting solution-adaptive and grid-fitted computational grid for the 0-deg angle-of-incidence case. For clarity, not all grid lines are shown. This figure illustrates the algorithm's ability to cluster points in regions of

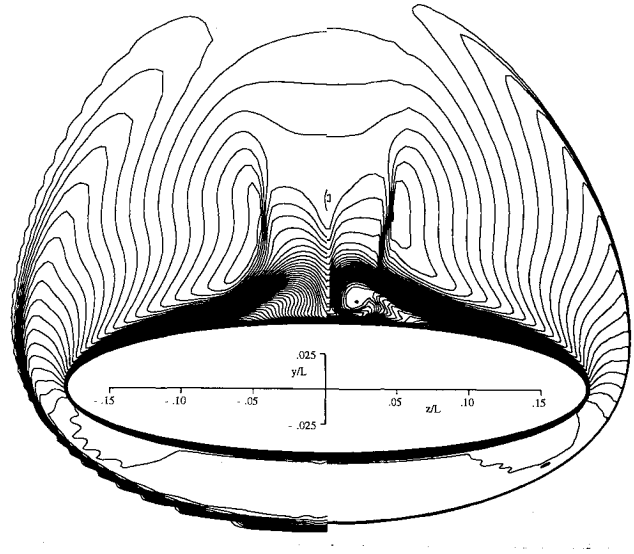

Fig. 8 Comparison of computed Mach number contours; left half, fixed grid; right half, solution adaptive and grid fitted (α = 15 deg, M_∞ = 7.4, $Re_{\infty,L} = 15 \times 10^6$, x/L = 0.667).

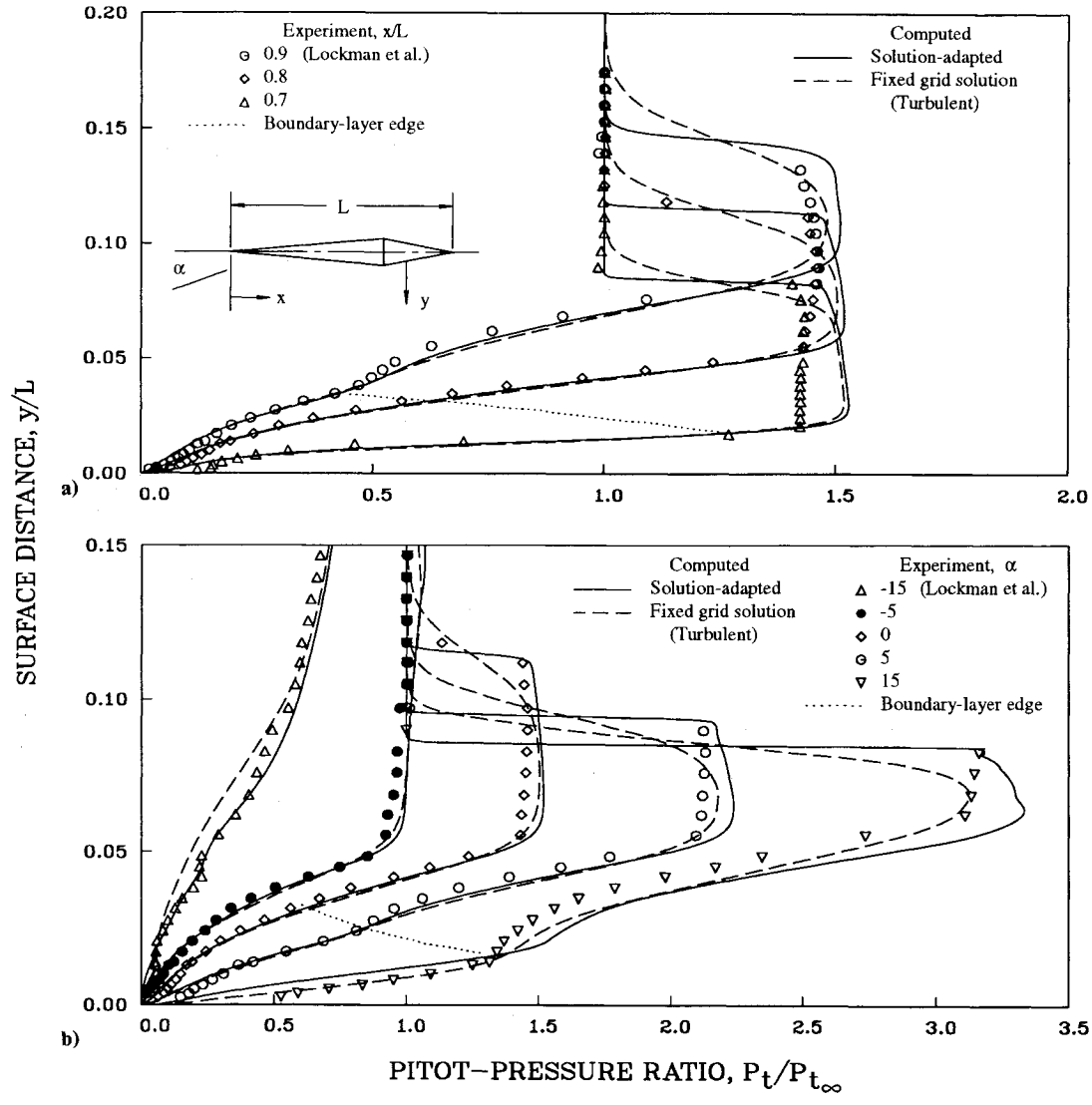

Fig. 9 Comparison of pitot pressure profiles: a) $\alpha = 0$ deg and b) $x/L = 0.8$.

interest and accurately align circumferential grid lines with the crossflow flowfield structure while also increasing grid point density. The far-field edge of the grid is accurately aligned with the bow shock whose position is indicated by the region of increased grid clustering.

The strategy in selecting the adaptation parameters can be best explained with reference to Fig. 3. The radial torsion parameter λ_ζ was set to a relatively smaller value (less resistance to grid point movement), and at the same time the radial grid straightness parameter C_ζ was set so as to enforce more grid straightness. At the same time, the circumferential torsion parameter λ_η was set to a higher value, with the circumferential grid straightness parameter C_η set to enforce more orthogonality. Using this set of parameters, grid points were permitted to move more freely during the radial adaptation sweeps, whereas more grid orthogonality is enforced on the circumferential sweeps. If strict orthogonality is imposed during both directional sweeps, more restriction in point movement occurs, resulting in a less adapted grid.

Figure 4 compares Mach number contours for solution-adaptive (right side) and fixed-grid (left side) cases at a crossflow location of $x/L = 0.667$. Significant improvement in the resolution of the bow shock can be seen. Small oscillations in the contours at the maximum spanwise location (near the crossflow stagnation point) can be seen in the fixed-grid half of the figure. These oscillations are not present in the solution-adaptive results; however, small oscillations appear just inside the bow shock for the solution-adaptive case.

Figure 5 compares a crossflow plane of the solution-adaptive and grid-fitted grid for the 5-deg angle-of-incidence case with a grid plane obtained without the use of the grid-fitting algorithm (left side). Additionally, the grid illustrated in the left half of Fig. 5 was computed using the torsional formulation of Ref. 2, whereas the grid in the right half of the figure was computed using the present torsional term formulation. For the left half of the figure (without grid fitting), the clustering at the bow shock has caused severe grid skewing. If the outer boundary of the grid is not grid fitted, then the radial extent of the freestream region compared with the radial extent of the region of interest can vary significantly at each circumferential location. This is clearly seen in the left half of Fig. 5 where, along the major axis, the extent of the freestream region is much larger than at other circumferential locations. Since the number of points in the freestream does not correspondingly increase with the freestream extent, the radial mesh spacing in the freestream along a radial outward line will be different at different circumferential locations. This causes the mesh in the freestream to distort, particularly when the radial extent of the freestream changes appreciably in the circumferential direction. Clearly, this is unacceptable, as seen in the left half of Fig. 5. The grid-fitting algorithm eliminates these problems by producing a crossflow grid plane whose shape is similar to that of the overall flow disturbance, thereby minimizing the number of points in the freestream.

For the solution-adaptive and grid-fitted case (right half of Fig. 5), the formulation described in the present paper with only

one torsional force term in the grid-adaptation equation was used. For the left half of Fig. 5, the formulation of Ref. 2 that includes two torsion force terms was used. These two terms, as discussed previously, can often oppose one another, producing grid skewness, the effects of which can be seen by comparing the differences in grid smoothness inside the bow shock (right and left halves of Fig. 5).

Grid skewness caused by the adaptation algorithm can adversely affect the quality of the solution. This is illustrated in Fig. 6, which compares computational grids and Mach contours at $x/L = 0.667$ near the crossflow stagnation point. Grid lines bulging outward from the bow shock region in Fig. 6b result in a grid distortion and inaccuracies in the predicted resolution and smoothness of the shock. In addition, the solution inside the shock also deteriorates. For the solution-adaptive and grid-fitted case shown in Fig. 6c, flow features are sharp and well resolved, illustrating the substantial improvements in accuracy over the solutions shown in Figs. 6a and 6b. The increased grid smoothness inside the bow shock of the solution-adaptive, grid-fitted case, compared with that in the grid of Fig. 6b, can be attributed to the combined effect of the reformulation of the adaptation equations to include a single torsion term (as discussed previously) and to the use of grid fitting.

Figure 7 illustrates a sectional view of the solution-adaptive and grid-fitted grid for the $\alpha = 15$ deg case. For clarity, every other circumferential grid line is plotted. The position of the bow shock is marked by the grid clustering region around the perimeter of the grid.

In Fig. 8, Mach number contours obtained using a solution-adaptive grid for the $\alpha = 15$ deg case are compared with Mach contours computed using a fixed grid (left half). The bow shock is clearly better resolved for the solution-adaptive case. The rather large angle of incidence results in a separated region on the leeward side that is better resolved due to the use of solution-adaptive gridding (right half of Fig. 8).

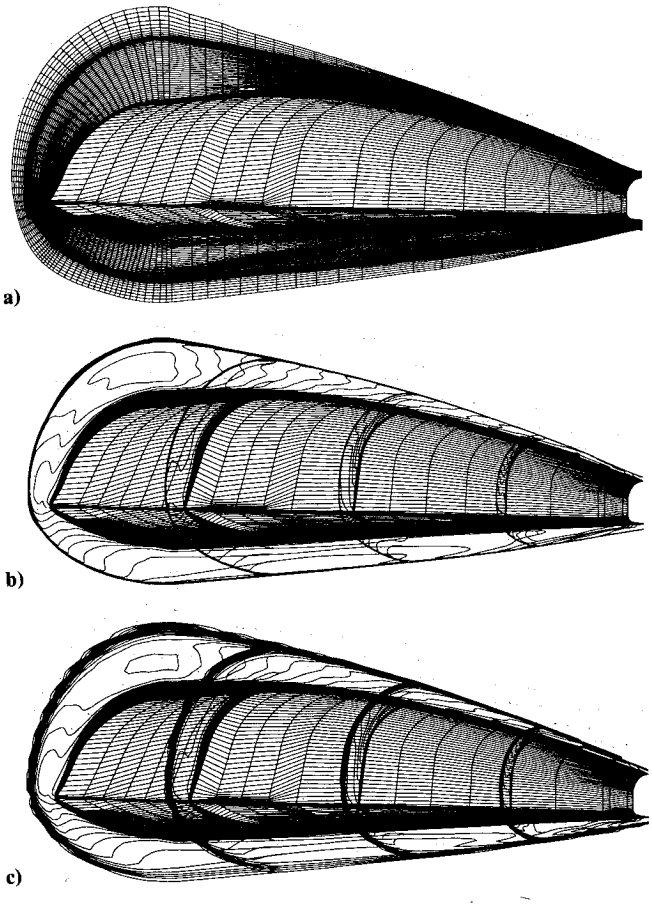

Fig. 10 Illustration of solution-adaptive and grid-fitted grid and Mach contours, $x = 0.04$–0.43 m: a) grid, b) Mach contours for solution adaptive and grid fitted, and c) Mach contours for fixed grid ($\alpha = 0$ deg, $M_\infty = 11.35$, $Re_L = 3.6 \times 10^7$/m, 65×65 crossflow grid).

In Fig. 9a predicted pitot pressure profiles obtained with a fixed grid and the solution-adaptive, grid-fitting algorithm are compared with experimental data at various x/L locations for the 0-deg angle-of-incidence case. Improvements are seen at each location in the resolution of the bow shock. Slight improvements can also be detected in the expansion region produced by the afterbody. The experimental data are taken from the study of Lockman et al.[15]

In Fig. 9b predicted pitot pressure profiles obtained with a fixed grid and the solution-adaptive, grid-fitting algorithm are compared with experimental data at $x/L = 0.8$ for the various angle-of-incidence cases studied. Again, significant improvements are detected near the bow shock on the windward side for both angles of incidence. Closer agreement with experiment is also observed for the solution-adaptive case compared with the fixed grid case in the expansion region on both the windward and leeward sides of the 5-deg angle-of-incidence case.

Computations were performed on the CRAY YMP/832 at NASA Ames Research Center. Total CPU requirements for each of the solution-adaptive cases took about 1.96 h or approximately 2.8 times the CPU time required for the fixed grid solutions. The solution-adaptive algorithm requires no significant increase in memory requirements over the fixed grid cases.

McDonnell Douglas Generic Option Vehicle

The solution-adaptive algorithm was also tested on the McDonnell Douglas generic option vehicle at 0-deg angle of incidence. Flowfield conditions used are: the freestream Mach number is $M_\infty = 11.35$, the freestream temperature is $T_\infty = 60.2$ K, the wall temperature is $T_w = 311.1$ K, the specific heat ratio is $\gamma = 1.4$, and the Prandtl number is $Pr = 0.72$. The unit Reynolds number, $Re = 35.98 \times 10^6$/m, is expressed per meter of the grid. The flow is turbulent and the eddy viscosity is computed using the algebraic model of Baldwin and Lomax.[16] A perfect gas is assumed, and transition to fully turbulent flow is assumed to occur at $x = 0.04$ m. Both solution-adaptive and fixed grids consist of 65 points in each crossflow direction.

Figure 10a illustrates the solution-adaptive and grid-fitted grid on the forebody of the generic option. As expected, the grid is clustered in the important regions. Figure 10b shows the solution-adaptive Mach contours, and Fig. 10c shows the corresponding contours on a fixed grid. The bow shock and the boundary-layer region are well resolved in both the upper and lower planes in Fig. 10b. The outer grid boundary, due to grid fitting, is accurately aligned with the bow shock. In Fig. 10c the fixed grid solution is clearly not as well resolved.

Figure 11 compares the fixed grid with solution-adaptive grids obtained both with and without the grid-fitting algorithm at the maximum spanwise location for a chord distance of 0.37 m. Also shown are computed Mach contours. The fixed grid solution of Fig. 11a shows a smeared bow shock, and the contours are wavy due to poor resolution. For the solution-adaptive case without grid fitting (Fig. 11b), although the shock is better resolved, the oscillations in the Mach contours are still evident. This is attributable to the grid lines distorting outside the bow shock regions as discussed for the all-body results. The solution-adaptive results with grid fitting (Fig. 11c) show significant improvements in the resolution of the bow shock region. The grid is smooth and reasonably orthogonal but provides the necessary clustering where required.

Figure 12 compares Mach number contours at three different x locations between $x = 0.43$ and 0.71 m computed using a fixed computational grid with those computed using a solution-adaptive grid. Mach contours in the lower symmetry plane of Fig. 12b, showing the interaction of the compression shocks, are well resolved by the use of the adaptive grid. The corresponding fixed grid contours exhibit considerable smearing of the bow and compression shocks due to lack of the necessary grid density in these regions. At the lower surface of the upstream-most contour section of Fig. 12b, the first compression shock can be seen just below the outer edge of the boundary layer. At the second cross-section this shock wave has moved away from the body surface and is about

midway between the body surface and the bow shock. The shock due to the second compression surface interacts with the bow shock at the location of the third set of cross-sectional Mach contours. Also enhanced by the solution-adaptive grid code is the shock interaction at the corner of the wing section of the third Mach contour section. The expansion fan resulting from the interaction of the two ramp shocks is clearly resolved in the solution-adaptive results. These features of the flow are not as easily recognizable in the Mach contours of Fig. 12a.

Summary

An improved solution-adaptive grid algorithm has been developed and applied to a parabolized Navier-Stokes solver. In the present work, the solution-adaptive grid procedures were modified

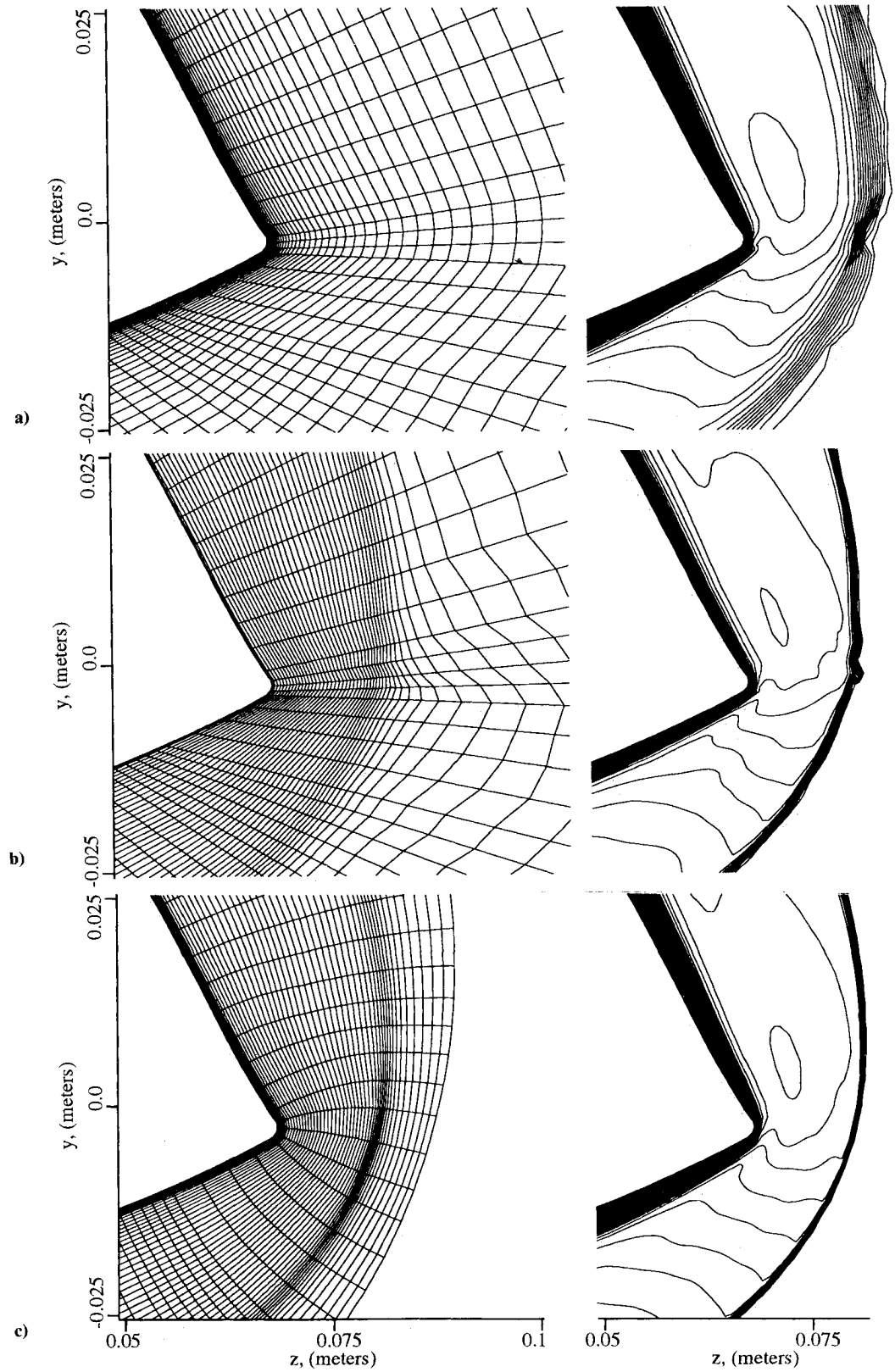

Fig. 11 Comparison of grids and Mach number contours near maximum spanwise location: a) fixed grid, b) adapted, with grid fitting, and c) adapted and grid fitted (α = 0 deg, M_∞ = 11.35, $Re_L = 3.6 \times 10^7$/m, 65 × 65 grid).

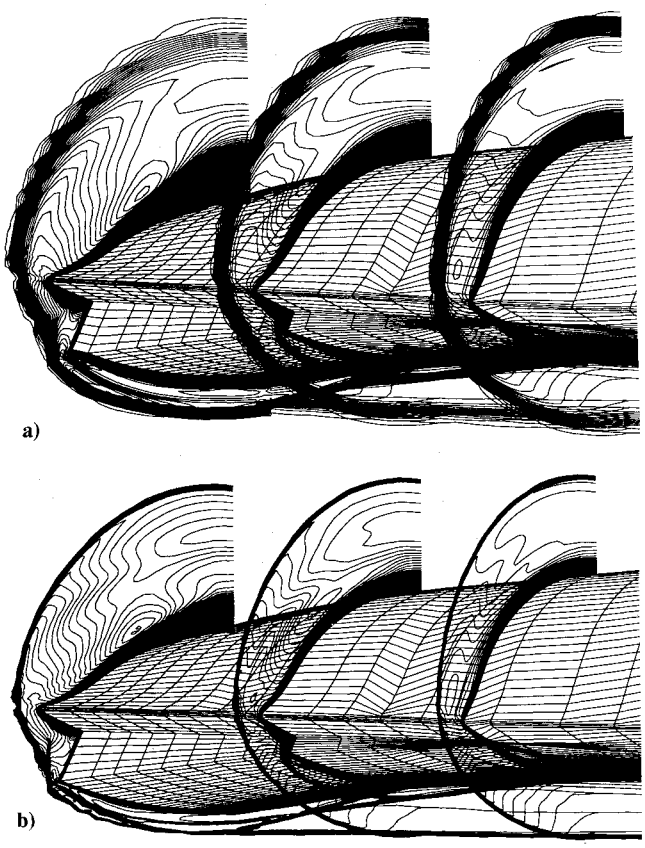

Fig. 12 Comparison of Mach number contours at $x = 0.43$ and 0.71 m for generic option vehicle: a) fixed grid and b) solution-adaptive grid ($\alpha = 0$ deg, $M_\infty = 11.35$, $Re_L = 3.6 \times 10^7$/m, 65×65 grid).

from those of Ref. 2 for application to more general three-dimensional configurations. These modifications included the formulation of a new technique to project the adaptive mesh plane downstream to the next marching station in preparation for the next step. A three-dimensional grid-fitting algorithm was also developed that enabled the solution-adaptive algorithm to provide a smoother adaptive grid. The torsional force term formulation of the system of grid-adaptation equations was also modified in the present work. This modification increased the usability of the algorithm by reducing the dependence of the user-selected adaptation parameters on the relative scales of the grid. This increased the range of usable parameters, thus reducing the number of trial solutions required for parameter adjustment.

The algorithm was then tested on the hypersonic flow over two lifting body configurations. The first was the Ames all-body vehicle, and flowfield results were computed at 0-, 5-, and 15-deg angles of incidence. Results computed using the solution-adaptive grid-fitting scheme were compared with those obtained using conventional fixed grids. Significant improvements were again observed in flowfield resolution as well as pitot pressure predictions. Results obtained using the grid-fitting scheme were also compared with results obtained without the use of grid fitting, and the advantages of grid fitting were clearly highlighted.

The adaptive algorithm was also tested on the McDonnell Douglas generic option vehicle. The complexity of the surface grid of this geometry was the major reason for the reformulation of the downstream grid-projection procedure. The flowfield results obtained using the adaptive algorithm illustrate the success of the grid-fitting and grid-projection methods developed in this work.

Acknowledgments

This work was supported by the Applied Computational Fluids Branch at NASA Ames Research Center under Joint Interchange NCA2-326 and NCA2-522. The authors wish to thank Branch Chief Terry L. Holst for the continued support and computer resources.

References

[1]Harvey, A. D., Acharya, S., Lawrence, S. L., and Cheung, S., "Solution Adaptive Grid Procedure for High-Speed Parabolic Flow Solvers," *AIAA Journal*, Vol. 29, No. 8, 1991, pp. 1232–1240.

[2]Harvey, A. D., Acharya, S., and Lawrence, S. L., "Solution-Adaptive Grid Procedure for the Three-Dimensional Parabolized Navier-Stokes Equations," *AIAA Journal*, Vol. 30, No. 4, 1992, pp. 953–962.

[3]Thompson, J. F., "A Survey of Dynamically-Adaptive Grids in the Numerical Solution of Partial Differential Equations," *Applied Numerical Mathematics*, Vol. 1, 1985, pp. 3–27.

[4]Hawken, D. F., "Review of Adaptive-Grid Techniques for Solution of Partial Differential Equations," Univ. of Toronto, Institute of Aerospace Studies, Review 46, Toronto, Ontario, Canada, Dec. 1985.

[5]Moukalled, F. H., "Adaptive Grid Solution Procedure for Elliptic Flows," Ph.D. Dissertation, Louisiana State Univ., Baton Rouge, LA, Dec. 1987.

[6]Gnoffo, P. A., "A Vectorized, Finite-Volume, Adaptive Grid Algorithm Applied to Planetary Entry Problems," AIAA Paper 82-1018, St. Louis, MO, June 1982.

[7]Nakahashi, K., and Deiwert, G. S., "A Practical Adaptive-Grid Method for Complex Fluid-Flow Problems," NASA TM-85989, June 1984.

[8]Nakahashi, K., and Deiwert, G. S., "Three-Dimensional Adaptive Grid Method," *AIAA Journal*, Vol. 24, No. 6, 1986, pp. 948–954.

[9]Davies, C. B., and Venkatapathy, E. W., "A Simplified Self-Adaptive Grid Method, SAGE," NASA TM-102198, Oct. 1989.

[10]Djomehri, D. J., and Deiwert, G. S., "Three-Dimensional Self-Adaptive Grid Method for Complex Flows," NASA TM-101027, Nov. 1988.

[11]Lawrence, S. L., "Application of an Upwind Algorithm to the Parabolized Navier-Stokes Equations," Ph.D. Dissertation, Iowa State Univ. of Science and Technology, Ames, IA, May 1987.

[12]Lawrence, S. L., Tannehill, J. C., and Chaussee, D. S., "An Upwind Algorithm for the Parabolized Navier-Stokes Equations," *AIAA Journal*, Vol. 22, No. 12, 1984, pp. 1755–1763.

[13]Lawrence, S. L., Tannehill, J. C., and Chaussee, D. S., "Application of an Upwind Algorithm to the Three-Dimensional Parabolized Navier-Stokes Equations," AIAA Paper 87-1112-CP, June 1987.

[14]Roe, P. L., "Approximate Riemann Solvers, Parameter Vectors, and Difference Schemes," *Journal of Computational Physics*, Vol. 43, No. 2, 1983, pp. 357–372.

[15]Lockman, W. K., Lawrence, S. L., and Cleary, J. W., "Experimental and Computational Surface and Flowfield Results for an All-Body Hypersonic Aircraft," AIAA Paper 90-3067, Aug. 1990.

[16]Baldwin, B. S., and Lomax, H., "Thin-Layer Approximation and Algebraic Model for Separated Turbulent Flows," AIAA Paper 78-257, Jan. 1978.

[17]Chakravarthy, S. R., and Szema, K. Y., "Euler Solver for Three-Dimensional Supersonic Flows with Subsonic Pockets," *Journal of Aircraft*, Vol. 24, No. 2, 1987, pp. 73–83.

[18]Vigneron, Y. C., Rakich, J. C., and Tannehill, J. C., "Calculation of Supersonic Viscous Flow over Delta Wings with Sharp Subsonic Leading Edges," AIAA Paper 78-1137, July 1978.

[19]Lawrence, S. L., "Comparison of the UPS Code with Experimental Data for the McDonnell Douglas Generic Option Vehicle," Fifth National Aerospace Plane Technology Symposium, Paper No. 78, October 1988.

[20]Thompson, J. F., Warsi, Z. U. A., and Mastin, C. W., *Numerical Grid Generation*, Foundations and Applications, North-Holland, Amsterdam, 1985.

[21]Anderson, D. A., Tannehill, J. C., and Pletcher, R. H., *Computational Fluid Mechanics and Heat Transfer*, Hemisphere, New York, 1984.

[22]Berger, M. J., and Jameson, A., "Automatic Adaptive Grid Refinement for the Euler Equations," *AIAA Journal*, Vol. 23, No. 5, 1985, pp. 561–586.

[23]Brackbill, J. U., "Coordinate System Control: Adaptive Meshes," *Numerical Grid Generation*, edited by J. F. Thompson, North-Holland, Amsterdam, 1982.

[24]Dwyer, H. A., Kee, R. J., and Sanders, B. R., "Adaptive Grid Method for Problems in Fluid Mechanics and Heat Transfer," *AIAA Journal*, Vol. 18, No. 12, 1980, pp. 1205–1212.

[25]Dwyer, H. A., "Grid Adaptation for Problems in Fluid Dynamics," *AIAA Journal*, Vol. 22, No. 8, 1984, pp. 955–960.

[26]Greenberg, J. B., "A New Self-Adaptive Grid Method," AIAA Paper 83-1934, 1983.

[27]Rai, M. M., and Anderson, D. A., "Application of Adaptive Grids to Fluid-Flow Problems with Asymptotic Solutions," *AIAA Journal*, Vol. 20, No. 4, 1982, pp. 496–502.